



1 Substantially positive contributions of new particle formation to Cloud Condensation
2 Nuclei under low supersaturation in China based on numerical model improvements
3
4 Chupeng Zhang^{1#}, Shangfei Hai^{2#}, Yang Gao^{1*}, Yuhang Wang^{3*}, Shaoqing Zhang^{4,2},
5 Lifang Sheng², Bin Zhao⁵, Shuxiao Wang⁵, Jingkun Jiang⁵, Xin Huang⁶, Aura Lupascu⁷,
6 Manish Shrivastava⁸, Jerome D. Fast⁸, Wenxuan Cheng¹, Xiuwen Guo¹, Ming Chu¹,
7 Nan Ma⁹, Juan Hong⁹, Qiaoqiao Wang⁹, Xiaohong Yao¹ and Huiwang Gao¹

8
9 ¹Frontiers Science Center for Deep Ocean Multispheres and Earth System, and Key
10 Laboratory of Marine Environmental Science and Ecology, Ministry of Education,
11 Ocean University of China, and Laoshan Laboratory, Qingdao, 266100, China

12 ²College of Oceanic and Atmospheric Sciences, Ocean University of China, Qingdao,
13 266100, China

14 ³School of Earth and Atmospheric Sciences, Georgia Institute of Technology, Atlanta,
15 GA, 30332, USA

16 ⁴Frontiers Science Center for Deep Ocean Multispheres and Earth System, and Key
17 Laboratory of Physical Oceanography, Ocean University of China, and Laoshan
18 Laboratory, Qingdao, 266100, China

19 ⁵State Key Joint Laboratory of Environment Simulation and Pollution Control, School
20 of Environment, Tsinghua University, Beijing, 100084 China, and State
21 Environmental Protection Key Laboratory of Sources and Control of Air Pollution
22 Complex, Beijing 100084, China

23 ⁶School of Atmospheric Sciences, Nanjing University, Nanjing, 210023, China

24 ⁷Institute for Advanced Sustainability Studies, Potsdam D-14467, Germany

25 ⁸Atmospheric Sciences and Global Change Division, Pacific Northwest National
26 Laboratory, Richland, WA, 99354, USA

27 ⁹Institute for Environmental and Climate Research, Jinan University, Guangzhou,
28 510000, China

29

30 # Authors contributed equally to this study.

31 *To whom correspondence to: yanggao@ouc.edu.cn, yuhang.wang@eas.gatech.edu

32

33

34

35



36

37

Abstract

38 New particle formation (NPF) and subsequent particle growth are important sources of
39 condensation nuclei (CN) and cloud condensation nuclei (CCN). While a number of
40 observations have shown positive contributions of NPF to CCN at low supersaturation,
41 negative NPF contributions were often simulated. Using the observations in a typical
42 coastal city of Qingdao, we thoroughly evaluate the simulated number concentrations
43 of CN and CCN using a NPF-explicit parameterization embedded in WRF-Chem model.
44 In terms of CN, the initial simulation shows large biases of particle number
45 concentrations at 10–40 nm (CN_{10-40}) and 40–100 nm (CN_{40-100}). By adjusting the
46 process of gas-particle partitioning, including mass accommodation coefficient of
47 sulfuric acid, the phase changes of primary organic aerosol emissions and the
48 condensational amount of nitric acid, the concomitant improvement of the particle
49 growth process yields a substantial reduction of overestimates of CN_{10-40} and CN_{40-100} .
50 Regarding CCN, SOA formed from the oxidation of semi-volatile and intermediate
51 volatility organic vapors (SI-SOA) yield is an important contributor. In the original
52 WRF-Chem model with 20 size bins setting, the yield of SI-SOA is too high without
53 considering the differences in oxidation rates of the precursors. Lowering the SI-SOA
54 yield results in much improved simulations of the observed CCN concentrations. On
55 the basis of the bias-corrected model, we find substantial positive contributions of NPF
56 to CCN at low supersaturation ($\sim 0.2\%$) in Qingdao and over the broad areas of China,
57 primarily due to the competing effects of increasing particle hygroscopicity surpassing
58 that of particle size decrease. This study highlights the potentially much larger NPF
59 contributions to CCN on a regional and even global basis.

60

61

62

63

64

65



66 **1. Introduction**

67 New particle formation (NPF) is a process in which gaseous vapors nucleate and
68 form critical molecular clusters, followed by subsequent growth to larger sizes through
69 condensation and coagulation (Kulmala et al., 2004; Kulmala et al., 2013; Lee et al.,
70 2019). Newly formed particles could effectively grow into the size of cloud
71 condensation nuclei (CCN) under certain supersaturation (SS), which exerts an impact
72 on the cloud microphysical process and global radiation balance (Merikanto et al., 2009;
73 Gordon et al., 2017; Kerminen et al., 2018; Ren et al., 2021). In addition, the high-
74 efficiency nucleation and explosive growth of particles may contribute to the formation
75 of haze (Guo et al., 2014), affecting air quality and human health (Yuan et al., 2015;
76 Chu et al., 2019; Kulmala et al., 2021).

77 The overestimate of condensation nuclei (CN) in numerical models are commonly
78 seen, despite the attempt to correctify the bias (Matsui et al., 2013; Arghavani et al.,
79 2022). It is a common way to reduce the nucleation rate which may reduce the particle
80 number concentration in proportion (Matsui et al., 2013). For instance, in the study of
81 NPF in East Asia in the spring of 2009, even after lowering the nucleation rate in a
82 regional model of WRF-Chem applied in their study, the reduced number concentration
83 of particles at 10–130 nm remained to be overestimated (Matsui et al., 2013). Using the
84 same regional model and a similar method to reduce the nucleation rate, Arghavani et
85 al. (2022) found particle number concentration at 10–100 nm was still overestimated
86 by nearly one order of magnitude, despite the effectiveness to reduce the overestimates
87 for the smaller particles such as 2.5–10 nm. In addition to the rate of NPF, the growth
88 process of particles also has a crucial effect on particle number concentration and size
89 distribution. In this process, the condensation of some chemical species such as sulfuric
90 acid, nitrate and organic gases on particles plays a major role in particle growth (Yao et
91 al., 2018; Lee et al., 2019; Li et al., 2022), and the uncertainty of their condensation
92 amount may lead to the bias of CN simulation.

93 In addition to CN, there are large discrepancies in the predicted CCN between the
94 numerical models and observational results. Furthermore, as an important source of
95 CCN (Merikanto et al., 2009), the contribution of nucleation to CCN quantified by



96 numerical models is also highly uncertain. For example, in terms of predicting CCN,
97 Fanourgakis et al. (2019) evaluated the CCN concentrations simulated by 16 global
98 aerosol–climate and chemistry transport models with observations at 9 sites in Europe
99 and Japan from 2011 to 2015, and found that all models underestimated CCN
100 concentrations with a mean normalized mean bias (NMB) of -36% at low
101 supersaturation ($SS=0.2\%$). Models also tend to underestimate the contribution of NPF
102 on CCN, especially at low supersaturation. The continuous observation of CCN
103 concentrations throughout the year (July 2008–June 2009) carried out in Hyytiälä,
104 Finland, showed that under low SS, nucleation enhanced the CCN by 106% and 110%
105 at $SS=0.1\%$ and 0.2% respectively (Sihto et al., 2011). Observations acquired in Beijing
106 from July 12 to September 25, 2008, also suggested that nucleation significantly
107 increases CCN at all supersaturations, even when supersaturation is low (i.e., 0.07%
108 and 0.26%). Thus, the occurrence of NPF enhanced CCN by a factor of 1.7 and 2.2,
109 respectively (Yue et al., 2011).

110 However, previous numerical experiments behave oppositely. For instance, Matsui
111 et al. (2011) quantified the contribution of nucleation to CCN using WRF-chem in
112 Beijing in August and September 2006 and found reduced CCN under low SS, e.g.,
113 when $SS=0.02\%$, the concentration of CCN is reduced by up to $\sim 50\%$. They attributed
114 this to the fact that the small particles produced by nucleation may inhibit the growth
115 of the preexisting particles (Matsui et al., 2011). Similarly, Dong et al. (2019) conducted
116 NPF simulations with the WRF-Chem for the summer of 2008 focusing on the Midwest
117 of the United States, and found that the nucleation resulted in decreased CCN at low
118 supersaturation ($SS=0.1\%$). Besides, a study carried out for East Asia in 2009 also
119 indicated that at low supersaturation (e.g. $SS=0.1\%$), nucleation has little impact on
120 CCN (Matsui et al., 2013). The contrasting effects of nucleation on CCN at low
121 supersaturations in model and observations is not explained in these previous studies.

122 At the stage of particle growth, secondary organic aerosol (SOA) formed by
123 atmospheric oxidation of organic vapors is a major contributor to particle growth to
124 CCN-related sizes (Liu and Matsui, 2022; Qiao et al., 2021). SOA formed by multi-
125 generational gas-phase oxidation of semi-volatile and intermediate volatility organic



126 compounds (S/IVOC) is called SI-SOA (Jimenez et al., 2009; Zhang et al., 2007). Zhao
127 et al. (2016) made a comprehensive assessment of the roles of various SOA precursors
128 in SOA formation in real atmosphere in China in 2010, and the results demonstrated
129 that evaporated POA and IVOC (i.e. S/IVOC) made a significant contribution to SOA,
130 contributing up to 82% to the average SOA concentration in eastern China. However,
131 the effect of SI-SOA on CCN has not been fully studied.

132 In this paper, WRF-Chem was applied to simulate the effect of the NPF on CCN
133 in Qingdao in February 2017. The simulated results from the WRF-Chem model are
134 firstly compared with observations in Qingdao, exhibiting large biases in CN. This is
135 followed by an improvement through a few processes. At the end, the impact of SI-
136 SOA yield and nucleation on CCN is investigated.

137 **2. Data and methods**

138 **2.1 Observations**

139 The measurements used in this study were carried out over the sampling site from
140 February 5 to 24, 2017 at the campus of Ocean University of China (36°09'37"N,
141 120°29'44"E) in Qingdao, which is surrounded by residential buildings and is situated
142 about 10 km away from the city center. A fast mobility particle sizer (FMPS, TSI Model
143 3091) was applied to measure the aerosol particle size distribution for the size range of
144 5.6 nm to 560 nm (Liu et al., 2014b). The size-resolved CCN activity is measured by a
145 cloud condensation nuclei counter (CCNc) at three different supersaturations (0.2%,
146 0.4% and 0.6%) and each supersaturation lasts for 5 minutes. More information about
147 the CCN measurement can be found in Li et al. (2015).

148 **2.2 Model configurations**

149 WRF-Chem version 3.9 is used to simulate NPF events, with the main physical
150 and chemical parameterization settings summarized in Table 1. The spatial resolution
151 is 36 km with 35 vertical layers and a model top at 50 hPa. A continuous run from
152 February 1 to 25, 2017, was conducted, with the first five-day results as the spin-up and
153 discarded in the analysis.

154



155

Table 1 WRF-Chem model configurations used in this work

	Model configuration
Microphysics	Morrison 2-moment microphysics scheme (Morrison et al., 2009)
Planetary Boundary Layer (PBL)	YSU boundary layer scheme (Hong et al., 2006)
Longwave and Shortwave Radiation	RRTMG longwave and shortwave radiation (Iacono et al., 2008)
Land model	Unified Noah Land Surface scheme (Chen and Dudhia, 2000; Tewari et al., 2016)
Cumulus	Grell-3D cumulus parameterization scheme (Grell, 1993)
Aerosol module	MOSAIC module (Zaveri et al., 2008; Matsui et al., 2011)
Gas-phase Chemistry	SAPRC-99 gas-phase chemistry scheme (Carter, 2000)

156

157 The meteorological initial and boundary conditions are driven by Climate Forecast
 158 System model version 2 (CFSv2; (Saha et al., 2014)) reanalysis developed by National
 159 Centre for Environmental Prediction (NCEP). The initial and boundary chemical
 160 conditions of WRF-Chem are provided by Community Atmosphere Model with
 161 Chemistry (CAM-Chem; (Buchholz et al., 2019)). Anthropogenic emissions for the
 162 year of 2017 are obtained from the Multiresolution Emission Inventory for China
 163 (MEIC, <http://www.meicmodel.org/>) emission dataset (Li et al., 2017; Zheng et al.,
 164 2018).

165 The Model for Simulating Aerosol Interactions and Chemistry (MOSAIC) was
 166 used to delineate dynamic gas-particle mass transfer to represent the condensation
 167 growth of aerosol (Zaveri et al., 2008). The gas-particle partitioning of gas species on
 168 particles is regulated by the mass transfer rate, which is related to mass accommodation
 169 coefficient (α), a parameter involved in the model representing the probability of gas
 170 molecules entering the bulk liquid phase (Pöschl et al., 1998). The original setting of α
 171 for all condensing species for all size bins a in MOSAIC is 0.1 (Zaveri et al., 2008). In



172 the default release of WRF-Chem, MOSAIC was implemented in the sectional
173 framework with aerosol size distributions divided into 4 or 8 size bins spanning 39 nm
174 to 10 μm in diameter. To explicitly express the nucleation and the growth of newly
175 formed particles, the aerosol size range in the MOSAIC module was extended from 1
176 nm to 10 μm , with the number of aerosol size bins increased to 20 (Matsui et al., 2011;
177 Matsui et al., 2013; Lupascu et al., 2015; Lai et al., 2022).

178 The chemical aging process of organic aerosols (OA) is modeled by the volatility
179 basis set (VBS) approach, which was widely used in air quality models to represent
180 complex mixtures of thousands of organic species (Donahue et al., 2006; Shrivastava
181 et al., 2011; Chrit et al., 2018). The VBS method classifies compounds according to the
182 effective saturation concentration (C^*), which represents the proportion of the
183 component in the gas phase to the particle phase (Donahue et al., 2006), and species
184 with higher C^* values are more volatile. The oxidation of highly volatile precursors to
185 form relatively low volatile components represents the aging process of OA. OA
186 consists of directly emitted primary organic aerosols and photochemically produced
187 secondary organic aerosols (SOA) (Shrivastava et al., 2011). In this study, the
188 simplified 2-species VBS mechanism was applied to the simulation of SOA, during
189 which primary organic aerosol was represented by two species based on volatility with
190 effective saturation concentration C^* values (at 298 K and 1 atm) of 10^{-2} and $10^5 \mu\text{g m}^{-3}$
191 m^{-3} (Shrivastava et al., 2011). Primary organic aerosols with C^* of $10^5 \mu\text{g m}^{-3}$ refers to
192 S/IVOC, which is in the gas phase under most atmospheric conditions due to its high
193 volatility, while for those primary organic aerosols with C^* of $10^{-2} \mu\text{g m}^{-3}$, is treated as
194 gas phase as well in the original model. The SOA formed by photochemical oxidation
195 of S/IVOC precursors is called SI-SOA and the SOA formed by oxidation of VOC
196 precursors is named V-SOA. In the simplified 2-species VBS mechanism, SI-SOA (C^*
197 of $10^{-2} \mu\text{g m}^{-3}$) is formed by the oxidation reaction of S/IVOC precursors (C^* of $10^5 \mu\text{g}$
198 m^{-3}) and OH with an oxidation rate constant of $4 \times 10^{-11} \text{ cm}^3 \text{ molec}^{-1} \text{ s}^{-1}$. A detailed
199 description of 2-species VBS mechanism can be found in Shrivastava et al. (2011).

200

201 **2.3 Model sensitivity formulations**



202 Three sets of sensitivity tests are designed and listed in Table 2. The purposes of
 203 the three sets of experiments are as follows: (1) Adjust the condensation growth process
 204 of ultrafine particles in WRF-Chem model (Base, MAC, POA, NOCD, RACD, with
 205 details in Table 2); (2) Explore the effect of SI-SOA yield on CCN (Low-Yield and
 206 High-Yield); (3) Study the effect of nucleation process on CCN under the change of SI-
 207 SOA yield (Low-Yield and High-Yield and their corresponding cases without
 208 nucleation parameterization, i.e., Low_nucoeff and High_nucoeff). Each scenario will be
 209 explained in conjunctions with the results.

210 Table 2 The sensitivity tests involved in this study

Purposes	Simulation scenarios	Description
Adjust the condensation growth process of ultrafine particles	Base	Simulation with the default setting with nucleation coefficient set as $2 \times 10^{-6} \text{ s}^{-1}$, the same as Lai et al. (2022)
	Mass accommodation coefficient (MAC)	It is the same as Base except that the mass adjustment coefficient (α) of gaseous sulfuric acid is adjusted from 0.1 to 0.65.
	POA emission phase (PEP)	It is the same as MAC except that the phase of POA is changed from gas phase to particle phase.
	No condensation (NOCD)	It is the same as PEP except that no NH_4NO_3 condenses on particles below 40 nm.
	Ratio method for condensation (RACD)	It is the same as PEP except that the condensation of NH_4NO_3 on particles below 40 nm is reduced according to the ratio of acid particles to total



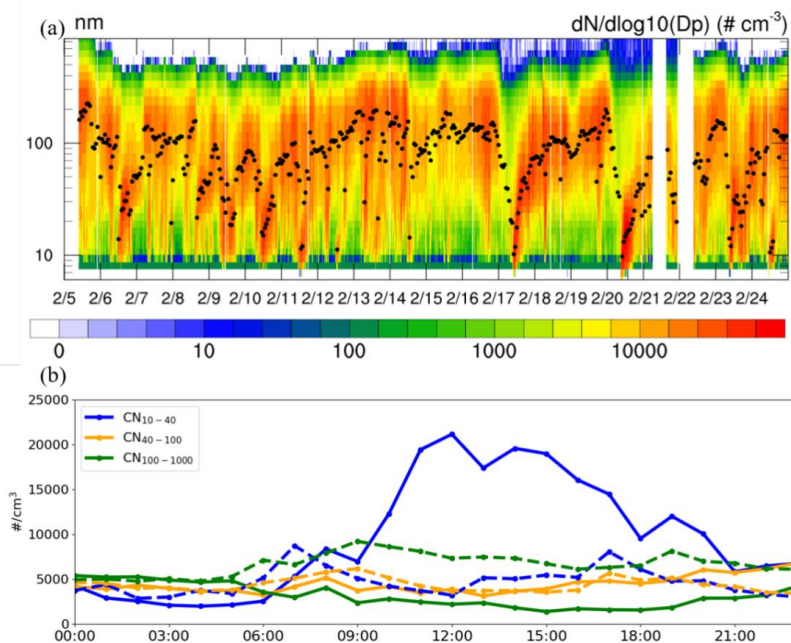
		particles reported in Wang et al. (2014).
Explore the effect of SI-SOA yield on CCN (Explore the effect of nucleation process on CCN under the change of SI-SOA yield)	High-Yield	Simulation with high oxidation rate of SI-SOA formation with reaction rate constant of $5 \times 10^{11} \text{ cm}^3 \text{ molec}^{-1} \text{ s}^{-1}$
	Low-Yield	Simulation with low oxidation rate of SI-SOA formation with reaction rate constant of $2 \times 10^{11} \text{ cm}^3 \text{ molec}^{-1} \text{ s}^{-1}$
Explore the effect of nucleation process on CCN under the change of SI-SOA yield	High_NUCOFF	Simulations without nucleation parameterizations based on High-Yield
	Low_NUCOFF	Simulations without nucleation parameterizations based on Low-Yield

211

212 3. Results

213 3.1 Observational analysis

214 Based on the criteria (Dal Maso et al., 2005; Kulmala et al., 2012), NPF is defined
 215 as an event with the emergence of a nucleation mode with particle diameters smaller
 216 than 25 nm, lasting for 2 hours or more, followed in general by a continuous particle
 217 growth. Six NPF events were identified in February 2017 in Qingdao, on the days of 6,
 218 9, 10, 17, 20 and 23 (Fig. 1a), yielding a frequency of ~30% and displaying a typical
 219 banana-shaped growth of particles in the particle number size distribution. Compared
 220 to a few other studies on NPF frequency in Qingdao, the results in this study are to a
 221 large extent consistent with that in the fall of 2012–2013 (30%; (Zhu et al., 2019)),
 222 slightly higher than that in summer 2016 (22%; (Zhu et al., 2019)) and lower than that
 223 in spring of 2010 (41%; (Liu et al., 2014c)). The higher frequency in spring in Qingdao
 224 is consistent with the observational results at different stations in the Northern
 225 Hemisphere in Nieminen et al. (2018).



226

227 Fig. 1 Distribution of particle number concentration. (a) Temporal evolution of particle
 228 size distributions (colored shading) and geometric median diameter (GMD; dots in
 229 black) in Qingdao on February 5-24, 2017. (b) The mean diurnal variation of CN_{10-40}
 230 (blue), CN_{40-100} (orange) and $CN_{100-1000}$ (green) composited during the NPF (solid lines)
 231 and non-NPF (dashed lines) days on February 5-24, 2017. All times are local times (LT)
 232

233 During the six NPF events identified in February in Qingdao, the mean diurnal
 234 cycle of CN_{10-40} (10–40 nm) particles exhibits triple peaks (solid blue in Fig. 1b), in the
 235 morning (8:00 LT), noon (12:00–14:00 LT) and evening (19:00 LT), respectively. A
 236 comparable three-peak feature was also observed in earlier years during 2016–2018 in
 237 Qingdao (Zhu et al., 2021). The morning and evening peaks of CN_{10-40} , with values of
 238 $\sim 5300 \text{ cm}^{-3}$ and $\sim 12000 \text{ cm}^{-3}$, respectively, are likely caused by the primary emissions
 239 from traffic and cooking activities (Wu et al., 2021a; Wang et al., 2022; Cai et al., 2020).
 240 The occurrence of NPF starts approximately at 9:00 am LT, accompanied by a
 241 substantial increase in CN_{10-40} compared with non-NPF days (solid vs. dashed lines, in
 242 blue), yielding a peak around noon (20000 cm^{-3} during 12:00–14:00 LT). In addition,



243 larger particles (e.g., CN_{40–100} and CN_{100–1000}) displayed a slow or no increase in the
244 afternoon.

245

246 **3.2 Model improvement in particle number concentration simulations**

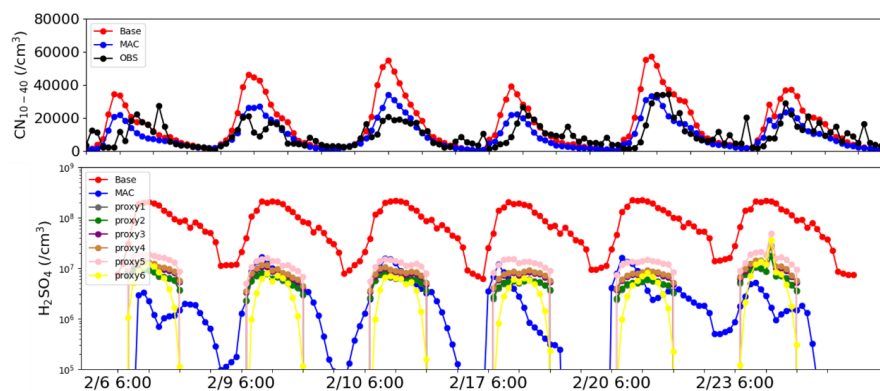
247 Particle number concentrations, primarily in two ranges of 10–40 nm and 40–100
248 nm, are commonly simulated with large biases. In the smaller size range (10–40 nm),
249 the particle number concentration is associated with NPF and particles growth. During
250 NPF, despite differences among the formation mechanisms, H₂SO₄ is considered the
251 common species (Yu, 2005; Lovejoy et al., 2004), which often suffer large biases (Cai
252 et al., 2016; Matsui et al., 2011). In the size range of 40–100 nm, the particle number
253 concentration is primarily affected by the condensation growth of particles below 40
254 nm, which is closely related to chemical components such as SOA and nitrate.

255 **3.2.1 Bias correction of particle number concentration at 10–40 nm**

256 In this study, as shown in Fig. 2, comparisons of CN_{10–40} between simulations (red
257 line in Fig. 2a) and observations (black line in Fig. 2a) results of the six NPF events
258 mentioned in the previous section in Qingdao in February 2017 indicate that model
259 overestimates CN_{10–40} with mean fractional bias (MFB) of 48%. As one of the major
260 processes affecting the particle number concentration of 10–40 nm, nucleation is
261 governed by the particle nucleation rate of 1 nm particles (cm⁻³ s⁻¹), which is closely
262 associated with the concentration of H₂SO₄. For instance, in a commonly applied
263 activation mechanism, the nucleation rate calculated by $J^* = K_{ACT} \times [H_2SO_4]$. Note
264 that K_{ACT} is the nucleation coefficient considering the physical properties and chemical
265 species of nucleation process under different environments, indicating that a lumped
266 chemical species are included in the scheme reflected primarily in the nucleation
267 coefficient k , set as $2 \times 10^{-6} \text{ s}^{-1}$ based on previous studies (Sihto et al., 2006; Riipinen
268 et al., 2007). Dong et al. (2019) simulated NPF occurring in the summer of 2008 in the
269 United States using the NFP-explicit WRF-Chem based on the activation mechanism,
270 which overestimated the particle number concentration at 10–63 nm by nearly doubled,
271 even when the K_{ACT} decreased by one order of magnitude (set at a very low value of
272 10^{-7} s^{-1}). Therefore, it is likely that the overestimation of particle number concentration



273 in the smaller particle size segment is probably due to the bias of simulated sulfuric
 274 acid.



275
 276 Figure 2 Time series of (a) CN_{10-40} on NPF days, where red and blue represent Base
 277 and MAC simulation results respectively, and black represents observation results, and
 278 (b) sulfuric acid gas concentration obtained by simulation and by proxies (dark grey:
 279 Eq. 1; green: Eq. 2; purple: Eq. 3; brown: Eq.4; pink: Eq.5; yellow: Eq.6). All times are
 280 in local times.

281

282 Measurement of sulfuric acid gases in the lower troposphere is challenging due to
 283 the generally low ambient concentration of sulfuric acid (10^6-10^7 molecule cm^{-3}).
 284 Different methods have been proposed to estimate ambient sulfuric acid concentrations
 285 based on observations such as SO_2 (Petäjä et al., 2009; Lu et al., 2019; Mikkonen et al.,
 286 2011). For instance, Petäjä et al. (2009) proposed a linear method to approximate
 287 observed H_2SO_4 concentration in Hyytiälä, southern Finland. Moreover, a recent study
 288 by Lu et al. (2019) proposed a nonlinear method to construct a number of proxies for
 289 gaseous sulfuric acid concentration (Eq. 1–5), indicating that compared to the linear
 290 method in Petäjä et al. (2009), the nonlinear relationship can provide more accurate
 291 H_2SO_4 concentration in Beijing during February–March 2018 period. In addition, we
 292 also used another sulfuric acid nonlinear proxy (Eq. 6) based on long-term observations
 293 in Germany, Finland, the United States, etc. (Mikkonen et al., 2011). In this study, we
 294 adopt the above six nonlinear proxy methods (referred as proxy1 to proxy6) to estimate
 295 H_2SO_4 in Qingdao.



296 $[H_2SO_4] = 515.74 \times [SO_2]^{0.38} \times \text{Radiation}^{0.14} \times CS^{0.03}$ (1)

297 $[H_2SO_4] = 280.05 \cdot \text{Radiation}^{0.14} [SO_2]^{0.40}$ (2)

298 $[H_2SO_4] = 9.95 \times [SO_2]^{0.39} \times \text{Radiation}^{0.13} \times CS^{-0.01} \times [O_3]^{0.14}$ (3)

299 $[H_2SO_4] = 14.38 \times [SO_2]^{0.38} \times \text{Radiation}^{0.13} \times [O_3]^{0.14}$ (4)

300 $[H_2SO_4] = 0.0013 \times [SO_2]^{0.38} \times \text{Radiation}^{0.13} \times CS^{-0.17} \times ([O_3]^{0.14} + [NO_x]^{0.41})$ (5)

301 $[H_2SO_4] = 8.21 \times 10^{-3} \times [SO_2]^{0.62} \times \text{Radiation} \times (CS \times RH)^{-0.13}$ (6)

302 where $[SO_2]$, $[O_3]$ and $[NO_x]$ (molecule cm^{-3}) represents concentration of
303 observed SO_2 , O_3 and NO_x , respectively. “Radiation” (W m^{-2}) is global radiation. RH
304 (%) is the relative humidity, and CS (s^{-1}) is the condensation sink, which is calculated
305 based on observed particle distribution.

306 The simulated H_2SO_4 concentration from the Base simulation (dots in Fig. 2b) is
307 compared with observations obtained by proxies (see Fig. 2b), indicating that Base
308 simulations apparently overestimate by one order of magnitude compared to the H_2SO_4
309 estimated by proxies. The overestimation has been frequently reported previously, i.e.,
310 over Beijing (Matsui et al., 2011), which ascribes the bias to the overestimation of the
311 SO_2 concentration. In a more recent study, the sensitivity of H_2SO_4 to SO_2 is tested, and
312 the result shows that even when SO_2 is reduced to an unrealistically low level, the
313 simulated H_2SO_4 is still more than one order of magnitude higher than the observed
314 value (Lai et al., 2022), suggesting that the SO_2 concentration cannot fully explain the
315 overestimates.

316 In addition to the precursor of H_2SO_4 , the mass accommodation coefficient (α),
317 representing the probability of impaction of a gaseous molecule on a liquid surface and
318 entering the bulk liquid phase, is another important factor affecting the concentration
319 of sulfuric acid gas. In the public release of WRF-Chem, α is typically set to a low value
320 of 0.1 for all gas species under different volatility during the condensation process,
321 including H_2SO_4 (Davidovits et al., 2004; Zaveri et al., 2008). Recent studies indicate
322 that the low α value may not be applicable to the low volatile gases, which tend to have
323 a mean α value of 0.7 and close to the unity (Krechmer et al., 2017). In fact, an earlier
324 study has indicated based on experimental determination, the mass accommodation
325 coefficient of H_2SO_4 vapor in sulfuric acid aqueous solution was measured, and the best



326 fit value was 0.65 (Pöschl et al., 1998). Accordingly, a sensitivity simulation was
327 conducted by adjusting the mass accommodation coefficient of H_2SO_4 from 0.1 to 0.65,
328 referred to as MAC.

329 This simulation brought the H_2SO_4 concentration (see Fig. 2b) much closer to the
330 calculated results from proxies, and the corresponding biases reduced by approximately
331 an order of magnitude. Notably, the MAC simulation decreases the overestimate of
332 sulfuric acid gas concentration, resulting in a lower particle formation rate. The MAC
333 simulation also significantly reduces overestimate of CN_{10-40} (Fig. 2b), and MFB
334 compared to observations decreases from 48% to 1%.

335

336 **3.2.2 Improvement of particle number concentration simulations at 40–100 nm**

337 The number concentration of particles in the 40–100 nm range is mainly affected
338 by the coagulation and condensation processes. While the coagulation process tends to
339 largely affect ultrafine particles below 10 nm than those with larger sizes (Wu et al.,
340 2011), the condensation growth of particles during gas-particle partitioning at sizes of
341 10–40 nm, to a large extent, governs the variations in number concentration of 40–100
342 nm particles. The condensation process is primarily controlled by gas-particle
343 partitioning of chemical species, which may change the chemical composition of
344 particles, such as organic compounds and inorganics including sulfate, nitrate and
345 ammonium.

346 Among the species contributing to the condensation growth of particles at 10–40
347 nm, the organic compounds with with C^* of $10^{-2} \mu\text{g m}^{-3}$ play the dominant role (Pierce
348 et al., 2011). In the current model setting, there is a total of two volatility sets, including
349 $10^{-2} \mu\text{g m}^{-3}$ and $10^5 \mu\text{g m}^{-3}$. The low volatile organic matter of $10^{-2} \mu\text{g m}^{-3}$ comes from
350 two gas-phase sources, including the direct emission of primary organic aerosol (POA)
351 and SOA formed from S/IVOC (SI-SOA), conducive to condensation on particles.
352 While the condensation of gaseous SOA is in general reasonable, the gas phase
353 emissions of POA may be problematic. For instance, previous studies suggested that
354 POA is in gas phase close to the emissions source, but with rapid dilution and cooling
355 in the atmosphere away from the source, most POA condenses to particle-phase (Roldin



356 et al., 2011b; Roldin et al., 2011a; Shrivastava et al., 2008). Therefore, away from the
357 emissions source POA, being in the particle phase, will not be involved in the growth
358 of newly formed particles. Therefore, we assume that low volatility POA is emitted in
359 the particle phase rather than the gas-phase, which caused different size distributions of
360 POA compared to when it was emitted in the gas-phase (Fig. S1a vs. Fig. S1b). Emitting
361 low volatility POA in the particle phase eliminates the unreasonable quasi-banana shape
362 pattern exhibiting concomitant growth of newly formed particles with increasing mass
363 concentration of POA.

364 The composition analysis (Fig. S1c) in the 10–40 nm particles mass from the
365 model results indicates that organic compounds mentioned above only account for 21%
366 of total mass (sulfates, nitrates, ammonium salts and organics) in this size range and the
367 dominant species is nitrate which accounts for 51% of total mass, exhibiting
368 inconsistencies with the previous studies which in general indicates a much smaller
369 contribution of nitrate. For instance, Liu et al. (2014a) suggested that over North China
370 Plain in summer 2009, organic matter accounted for 77% of particles around 30 nm,
371 while the sum of SO_4^{2-} , NO_3^- and NH_4^+ only accounted for 18%. Another study showed
372 that nitrate accounted for 7–8% at urban sites and 17% at rural sites for particles mass
373 in 7–30 nm in the United States in 2007 (Bzdek et al., 2012). Therefore, the potentially
374 too high modeled nitrate fraction in 10–40 nm in this study is tightly associated with
375 the condensation process, with the specific reasons explained below.

376 The condensation of nitric acid on particles is highly constrained by the particle
377 acidity. The acidity in smaller particles (i.e., 10–40 nm) tends to be higher than that in
378 large particles, primarily due to the larger condensation of H_2SO_4 (Lu et al., 2022), and
379 particles with sizes greater than 40 nm have a much weaker acidity or are nearly neutral.
380 For example, observed evidence has shown that acidic ultrafine particles account for a
381 large proportion of ultrafine particles from 22 December 2010 to 15 January 2011 in
382 Hong Kong, e.g., 65% for particles within 5.5–30 nm (Wang et al., 2014).

383 In the model, a particle is determined to be in solid phase when the ambient relative
384 humidity is lower than the mutual deliquescence relative humidity of the particles
385 (Zaveri et al., 2005; Zaveri et al., 2008), which is in general suitable for particles



386 dominated by inorganics. In the study area, the results indicate that at most conditions
387 relative humidity are relatively low and the particles are in solid phase, in which the
388 condensation process is not affected by particle acidity and the condensation of nitric
389 acid on particles is directly calculated based on the gas-particle equilibrium
390 concentration (Zaveri et al., 2008). However, for particles below 40 nm, the main
391 compositions are likely to be organic matter (Zhu et al., 2014; Ehn et al., 2014), which
392 tends to be in liquid phase (Virtanen et al., 2011; Cheng et al., 2015), under which the
393 condensation of nitric acid is strongly constrained by acidity. Therefore, the phase
394 misrepresentation ignores the weakening effect of acidity on nitric acid condensation,
395 resulting in too high nitrate therein.

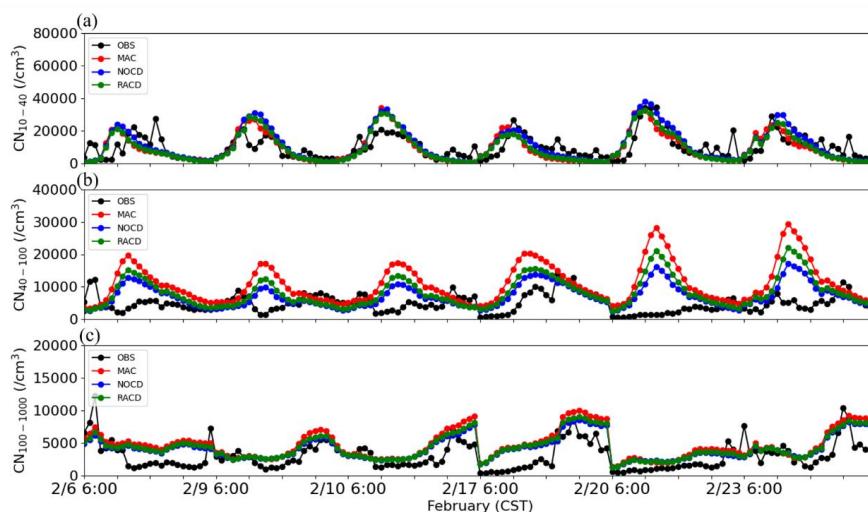
396 To overcome this issue, we propose a ratio method for condensation (RACD) to
397 partition the condensation of nitric acid on particles under 40 nm, by applying a ratio
398 of the number concentration of non-acidic particles to ultrafine particles. The method
399 is based on two assumptions, including: 1) little condensation of nitric acid on particles
400 with strong acidity (Lu et al., 2022); 2) the condensation of nitric acid on particles is
401 proportional to the ratio of the number concentration of non-acidic ultrafine particles to
402 the total particles, despite the existence of uncertainties. Fig. S2 depicts the average
403 particle number concentration and acid particle in the 1 to 40 nm range, calculated based
404 on Wang et al. (2014). The ratio of non-acidic particles is 8% for particles below 10 nm,
405 18% for particles at 10–15.8 nm, 30% for particles at 15.8–25.1nm, and 55% for
406 particles at 25.1–39.8 nm (Fig. S2). Note that the ratio is based on measurements
407 acquired at a single site in Hong Kong, therefore more observational studies are needed
408 to warrant the robustness of the method. Alternatively, the condensation of nitric acid
409 on particles in bins from 1nm to 40 nm is completely suppressed, referred to as NOCD.

410 The simulation results based on the two methods (RACD and NOCD) are shown
411 in Fig. 3. Compared to MAC, RACD simulations reduce previously noted
412 overestimation of PNC in the 40–100 nm size range (Fig. 3b), with the MFB decreases
413 from 83% to 63%. In addition to the amount of nitrate condensation during particle
414 growth mentioned above, the overestimation of particle number concentrations in the
415 40–100 nm range may be attributed to nucleation process. More specifically, in the



416 H₂SO₄-H₂O binary nucleation mechanism used in this study, when the concentration of
417 sulfuric acid gas is reduced (Section 3.2.1), the resulting decrease in nucleation rate
418 leads to a slight decrease in particle number concentration at 40–100 nm relative to
419 Base (MFB from 98% to 83%). Apart from that, it may also be related to the choice of
420 nucleation parameterization scheme. For example, using a global chemical transport
421 model GEOS-Chem, Yu et al. (2015) overestimated the concentration of particles in the
422 10–100 nm range by 161% at nine sites in the summer in North America. A possible
423 explanation for this overestimation was given by the uncertainty of the predicted
424 concentration of organic compounds involved in organics-mediated nucleation
425 parameterization. After they switched to another scheme of the ion-mediated nucleation
426 mechanism without organic matter, the number becomes 27% lower than the
427 observations (Yu et al., 2015). The test based on different schemes is beyond the scope
428 of the study, which is therefore not investigated.

429 Moreover, the overestimation of particles over 100 nm (CN_{100–1000}; Fig. 3c), which
430 have a strong influence on CCN, also decrease in the RACD simulation. Thus, the MFB
431 decreases from 25% (MAC) to 1%. Note that the slight increase of CN_{10–40} through the
432 application of RACD, can be linked to the decrease of nitrate condensation, and leads
433 to weakened particle growth and enhanced particle number concentration at 10–40 nm
434 (Fig. 3a). The alternative method by completely removing the nitrate condensation
435 (NOCD) yields even better performance in particle number concentration of 40–100
436 nm (MFB of 34%), indicating the feasibility by reducing the nitrate condensation. The
437 proportion of nitrate simulated by RACD is 23%, closer to values reported in past
438 observations (Bzdek et al., 2011; Bzdek et al., 2012), while the nitrate (1%) in the
439 scenario of NOCD seems to be too low. Considering the limited observational
440 information obtained based on previous studies, RACD is applied in this study.



441

442 Figure 3 The time series of (a) CN_{10-40} , (b) CN_{40-100} and (c) $CN_{100-1000}$ on NPF days in
 443 Qingdao on February 5-24 simulated MAC (marked in red), NOCD (marked in blue)
 444 and RACD (marked in green) as well as from observations (OBS) (marked in black).
 445 All times are local time.

446

447 3.3 Substantial contributions of SI-SOA to CCN

448 Compared with the original model setting, after adjusting the growth process of
 449 ultrafine particles (RACD), the number concentration of particles tend to decrease,
 450 especially for particles above 40 nm. Ultrafine particles above 40 nm are important
 451 sources of CCN (Dusek et al., 2006), in this way, the number concentration of CCN
 452 also tends to decline. In addition, in the Base case, we found that the model
 453 overestimated $CCN_{0.4\%}$ and $CCN_{0.6\%}$, with MFB being 64% and 87%, respectively.
 454 After adjusting the condensation growth process of ultrafine particles, under high
 455 supersaturation (i.e., $CCN_{0.4\%}$ and $CCN_{0.6\%}$), the capability of the model in reproducing
 456 the CCN is improved. RACD reduces the overestimation of $CCN_{0.4\%}$ and $CCN_{0.6\%}$, with
 457 MFB reduced to 30% and 56%, respectively, although the overestimates still exist (Figs.
 458 S3b, c). However, for low supersaturation (i.e., $CCN_{0.2\%}$), the decrease of number
 459 concentration of CCN is too large, and MFB decreases from 7% to -45% (Figs. S3a),
 460 therefore the bias will be further adjusted later.



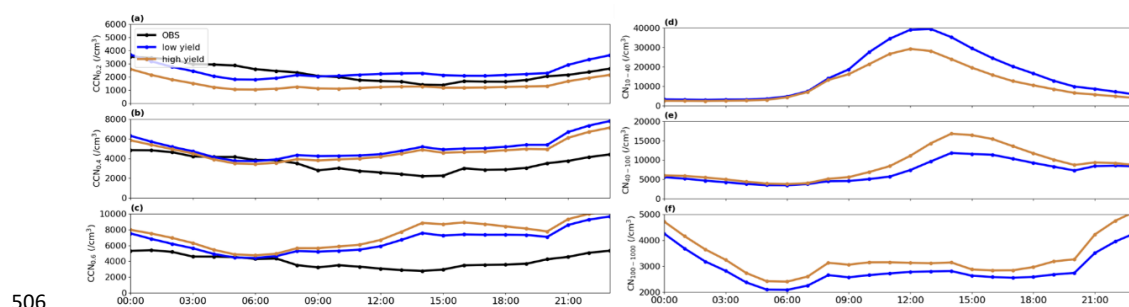
461 In addition to the growth process, the remaining overestimate of CCN under high
462 SS and underestimate of CCN over low SS is likely to be influenced by the chemical
463 compositions involved in the activation of ultrafine particles into CCN. Specifically,
464 ultrafine particles can grow up to CCN size under certain SS (Pierce and Adams, 2007).
465 This process is influenced by both particle size and hygroscopicity, and hygroscopicity
466 is closely related to the chemical composition of particles (Petters and Kreidenweis,
467 2007). In particular, inorganic compounds generally increase particle hygroscopicity,
468 increasing CCN. SOA has dual effects on CCN since it decreases particle
469 hygroscopicity but also promotes growth of particles, and these two effects are
470 competitive with each other (Wu et al., 2015; Zaveri et al., 2021). Ultrafine particles
471 must grow to a critical size to be activated into CCN (Dusek et al., 2006). SOA act as a
472 major contributor in promoting the condensational growth of ultrafine particles to the
473 critical size, facilitating particles activation into CCN. In contrast, SOA tends to reduce
474 the hygroscopicity of particles, leading to a diminished ability of activation to CCN
475 (Wu et al., 2015). These two competing effects work together and modulate the number
476 of CCN. Moreover, considering that SI-SOA is the main SOA component on ultrafine
477 particles (Fig. S3d), the effect of SI-SOA on CCN is therefore explored in this study.

478 Considering SI-SOA is a product of S/IVOC oxidation, the oxidation rate of
479 S/IVOC is tightly associated with CCN, which likely affects the bias of CCN. In the
480 original model setup, the oxidation rate is set to be a constant of $4 \times 10^{-11} \text{ cm}^3 \text{ molec}^{-1}$
481 s^{-1} for all S/IVOC. However, a recent study (Wu et al., 2021b) proposed that the
482 oxidation rate can be as high as $5 \times 10^{-11} \text{ cm}^3 \text{ molec}^{-1} \text{ s}^{-1}$ such as for polycyclic aromatic
483 hydrocarbons (PAHs), close to the original model value, but can be as low as half (i.e.,
484 $2 \times 10^{-11} \text{ cm}^3 \text{ molec}^{-1} \text{ s}^{-1}$) of the original modeling setting for S/IVOC species except
485 PAHs (O-S/IVOCs). It is noteworthy that the oxidation rates of 5×10^{-11} and 2×10^{-11}
486 in general represent the upper and lower bounds (Zhao et al., 2016; Wu et al., 2021b).

487 To delve into how oxidation rates affect CCN, we set up a few numerical
488 experiments (Table 2) to investigate the response of CCN to the oxidation rate of
489 S/IVOC at three supersaturations (0.6%, 0.4%, 0.2%), including cases of High_Yield
490 and Low_Yield. As it is shown in Fig. 4, decreasing the oxidation rate (Low_Yield)



491 leads to a reduction of ~10% of CCN at high supersaturation (i.e., CCN_{0.6%}) as
 492 compared to the High_Yield simulation. This behaviour is a consequence of the
 493 decrease of particle number concentrations associated with Low_Yield, particular of
 494 the particles close to the critical diameter (40–100 nm). In this case, the effect of particle
 495 size dominates the hygroscopicity. In contrast, at a lower supersaturation (CCN_{0.2%}),
 496 CCN increases by 42% when the oxidation rate is switched from a high to a low value,
 497 which is due to the smaller fraction of SI-SOA contributing to particulate mass when
 498 the oxidate rate is low. In this case, relative to SOA, a larger fraction of other particle
 499 constituents such as inorganics, increase the volume weighted particle hygroscopicity
 500 (Dusek et al., 2006) which causes the increase of CCN number. This means that the
 501 effect of hygroscopicity on CCN surpasses the influence on particle size at low
 502 supersaturations. This conclusion is consistent with the observation conducted by Ma
 503 et al. (2016) in the North China Plain in 2013, which suggested that along with the
 504 decrease of SS, the particles that can be activated to CCN is more sensitive to changes
 505 of particle hygroscopicity.



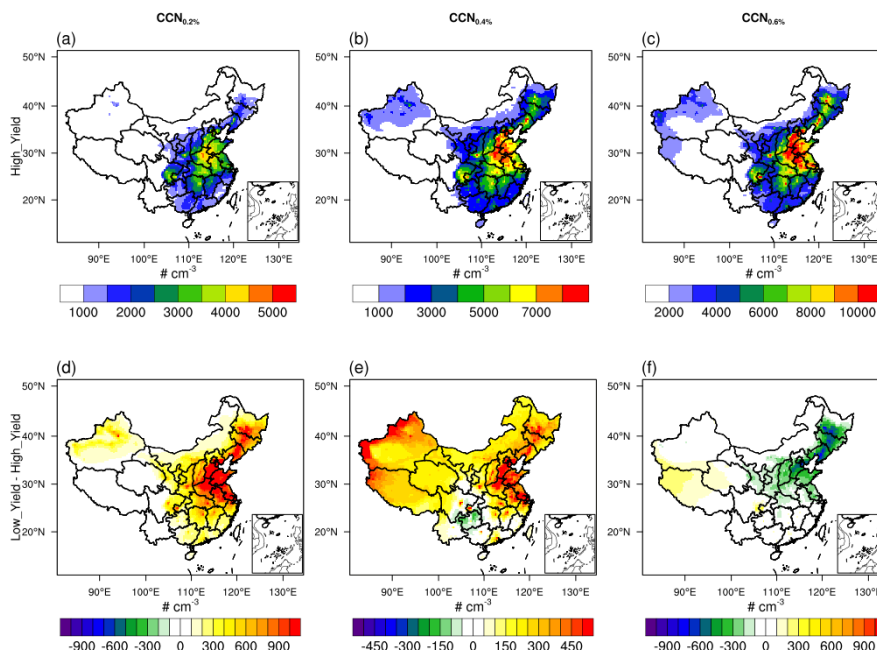
506
 507 Figure 4 Average diurnal variation of (a) CCN_{0.2%}, (b) CCN_{0.4%} and (c) CCN_{0.6%}
 508 and (d) CN₁₀₋₄₀, (e) CN₄₀₋₁₀₀, (f) CN₁₀₀₋₁₀₀₀ on NPF days in Qingdao on February 5-24,
 509 2017, in Low-yield and High-yield simulations, shown as blue and brown lines, and
 510 black lines represent observation results.

511
 512 Furthermore, compared to the high yield of SI-SOA, the low SI-SOA yield results
 513 in a high CCN concentration under low SS and low CCN concentration under high SS.
 514 Therefore, both the underestimates of CCN_{0.2%} (MFB of -45%) and overestimates of



515 CCN_{0.6%} (MFB of 56%) mentioned above are improved, with MFB of CCN_{0.2%} and
516 CCN_{0.6%} reaching 7% and 43%, respectively (Figs. 4a,c). This result suggests that the
517 oxidation rate of S/IVOC is possibly closer to the low value, which is understandable
518 based on Wu et al. (2021b), who found that the amount of O-S/IVOCs, which
519 corresponds to a low oxidation rate, is in general much larger (i.e., 20 times) than that
520 of PAHs with a high oxidation rate.

521 In addition to the single site of Qingdao, we further explore the impact of SI-SOA
522 yield on CCN from a larger spatial coverage (Fig. 5). Consistent with the mechanism
523 revealed over Qingdao, even from a larger spatial perspective, a lower oxidation rate of
524 S/IVOC essentially enhances CCN at a lower SS (e.g., CCN_{0.2%}; Fig. 5a) with the
525 highest increase over north China Plain area (Figs. 5a), and weakens CCN (i.e., by 10–
526 20% over Beijing-Tianjin-Hebei) at a higher SS (Figs. 5c), particularly over the dense
527 emission area (Fig. S4). It is worth noting that in the 2-species VBS mechanism used
528 in our study, all S/IVOC in the inventory is calculated based on a constant emission
529 ratio of S/IVOC to POA from all source categories (Shrivastava et al., 2011), which
530 may miss part of S/IVOC due to different emission ratios of POA from different source
531 (Chang et al., 2022).



532

533 Figure 5. Spatial distributions of CCN concentrations at different supersaturations (SS),
 534 (a) and (d) are $CCN_{0.2\%}$, (b) and (e) are $CCN_{0.4\%}$, and (c) and (f) are $CCN_{0.6\%}$. The top
 535 panels exhibit the results from the High_Yield simulation, and the bottom panels shows
 536 the difference between the Low_Yield and High_Yield simulations.

537

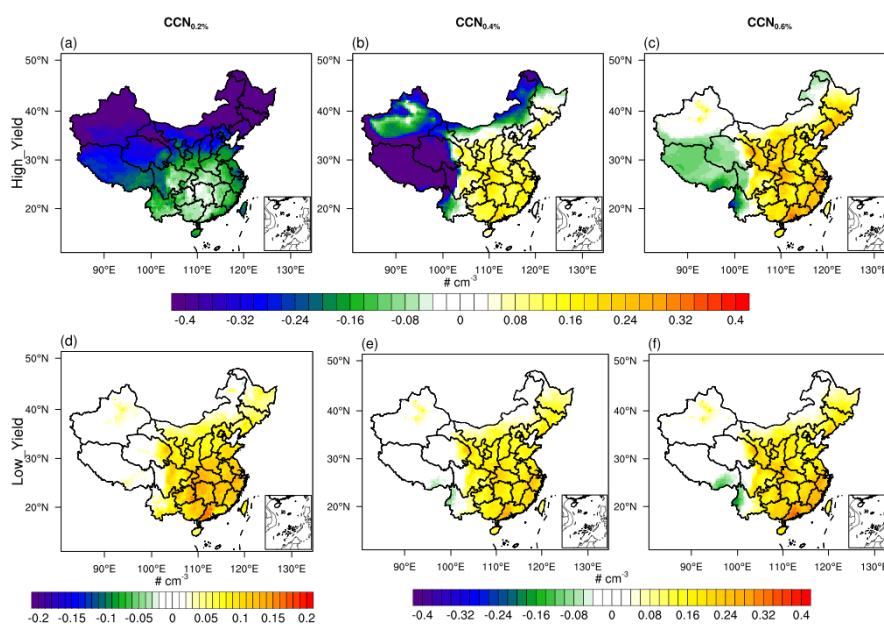
538 3.4 Contribution of nucleation to CCN under different SI-SOA yields

539 Considering the importance of nucleated particles on CCN (Yu et al., 2020;
 540 Westervelt et al., 2013), we further investigate the influence of nucleation on CCN
 541 under different SI-SOA yield conditions discussed above.

542 As shown in Fig. 6, in simulations close to the original model setting (High_Yield),
 543 when SS is low (i.e., $SS=0.2\%$), the nucleation process tends to reduce the CCN by
 544 ~10–50%. In contrast, when the SS is high (0.6%), the nucleation results in a significant
 545 increase in CCN in most regions of China. When the yield of SI-SOA is adjusted to a
 546 lower level, the nucleation process has a positive contribution to CCN under both low
 547 and high SS. Especially, when SS is low (0.2%), the sign reversal, i.e., from negative
 548 (Fig. 6a) to positive (Fig. 6d) contribution of NPF to CCN along with the decrease of
 549 SI-SOA yield, i.e., the increase is concentrated in the eastern China with an average of



550 10–20%. The primary mechanism lies in that along with the decrease of SI-SOA yield,
 551 the smaller fraction of SI-SOA yields an increase in hygroscopicity, which surpasses
 552 the suppression effect on particle growth due to reduced SI-SOA formation. In the real
 553 atmosphere, when the supersaturation is usually low, e.g. about ~0.1% in polluted areas
 554 (Kalkavouras et al., 2019; Hudson and Noble, 2014), CCN will likely reduce with
 555 increasing oxidation rate of S/IVOC and corresponding SI-SOA formation.



556
 557 Figure 6. Spatial distribution of contribution of nucleation to CCN calculated by the
 558 ratio of the difference between the parameterization with and without nucleation to the
 559 parameterization with nucleation under different SI-SOA yields in China in February
 560 2017. (a), (d) is CCN_{0.2%}, (b), (e) is CCN_{0.4%}, (c), (f) is CCN_{0.6%}. The upper panel and
 561 lower panel represent High_Yield and Low_Yield simulation respectively.

562

563

564

565 Conclusions

566 In this study, WRF-Chem explicit-NPF simulations are used to investigate the
 567 observed wintertime NPF events and their contribution to CCN in China. Based on



568 observations in a typical coastal city of Qingdao, we identify high biases of the model
569 simulated CN and CCN concentrations. Therefore, we updated and improved the
570 parameterization setting on particle growth in the model, mainly including: (1)
571 adjusting the mass accommodation coefficient (α) to from the default value of 0.1 to
572 0.65, an important parameter for sulfuric acid condensation; (2) proportionally reducing
573 the condensation amount of nitric acid on particles below 40 nm, (3) changing the
574 emitted low-volatility POA from gas to particle. Through these adjustments, the
575 capability of the model in reproducing CN and CCN is substantially improved, leading
576 to better agreement with the observed results, which significantly reduces the
577 overestimation of CN₁₀₋₄₀ (MFB decreases from 48% to 1%) and CN₄₀₋₁₀₀ (MFB
578 decreases from 98% to 63%).

579

580 For CCN, due to the crucial role of SI-SOA in promoting the growth of ultrafine
581 particles, on the basis of previous studies, we lower the oxidation rate of S/IVOC and
582 hence the production rate of SI-SOA, which weakens the growth of particles to reach
583 the critical size of CCN activation, but enhances particulate hygroscopicity favoring the
584 activation to CCN. When the yield of SI-SOA is adjusted to the lower bound of
585 literature value, CCN_{0.6%} is reduced by ~10% and is closer to observations. At low SS
586 (CCN_{0.2%}), the decrease of SI-SOA yield has greater effects on the increase of particle
587 hygroscopicity compared to the effect of the reduction of particle size due to the
588 decrease of condensation growth. It results in an increase of CCN (as large as ~42%) in
589 better agreement with observations. Under low SS conditions, common in the
590 atmosphere, a 2.5-fold reduction in SI-SOA yield results in a substantial increase of
591 CCN that switches from a negative contribution of new particle formation to CCN from
592 -50%~-10% to a positive contribution of 10~20%.

593

594 **Competing interests.** At least one of the (co-)authors is a member of the editorial board
595 of Atmospheric Chemistry and Physics.

596



597 **Acknowledgements.** This research was supported by grants from the National Natural
598 Science Foundation of China (42122039) and Fundamental Research Funds for the
599 Central Universities (202072001). Y.W. was supported by the National Science
600 Foundation Atmospheric Chemistry Program. M.S. was supported by the U.S.
601 Department of Energy (DOE) Office of Science, Office of Biological and
602 Environmental Research (BER) through the Early Career Research Program and the
603 Atmospheric System Research (ASR) program.

604

605

606 **References:**

- 607 Arghavani S, Rose C, Banson S, et al. 2022. The Effect of Using a New Parameterization of Nucleation in
608 the WRF-Chem Model on New Particle Formation in a Passive Volcanic Plume. *Atmosphere* [J],
609 13(1): 15.
- 610 Buchholz R R, Emmons L K, Tilmes S 2019. The CESM2 Development Team., 2019. CESM2.1/CAM-Chem
611 Instantaneous Output for Boundary Conditions. UCAR/NCAR - Atmospheric Chemistry
612 Observations and Modeling Laboratory.
- 613 Bzdek B, Zordan C, Luther G, et al. 2011. Nanoparticle Chemical Composition During New Particle
614 Formation. *Aerosol Science and Technology* [J], 45(1041-1048.
- 615 Bzdek B R, Zordan C A, Pennington M R, et al. 2012. Quantitative Assessment of the Sulfuric Acid
616 Contribution to New Particle Growth. *Environmental Science & Technology* [J], 46(8): 4365-
617 4373.
- 618 Cai C, Zhang X, Wang K, et al. 2016. Incorporation of new particle formation and early growth treatments
619 into WRF/Chem: Model improvement, evaluation, and impacts of anthropogenic aerosols over
620 East Asia. *Atmospheric Environment* [J], 124(262-284.
- 621 Cai J, Chu B, Yao L, et al. 2020. Size-segregated particle number and mass concentrations from different
622 emission sources in urban Beijing. *Atmos. Chem. Phys.* [J], 20(21): 12721-12740.
- 623 Carter W 2000. Documentation of the SAPRC-99 Chemical Mechanism for VOC Reactivity Assessment.
624 Final Report to California Air Resources Board [J].
- 625 Chang X, Zhao B, Zheng H, et al. 2022. Full-volatility emission framework corrects missing and
626 underestimated secondary organic aerosol sources. *One Earth* [J], 5(403-412.
- 627 Chen F, Dudhia J 2000. Coupling an Advanced Land-Surface/Hydrology Model with the Penn State/NCAR
628 MM5 Modeling System. 129(
- 629 Cheng Y, Su H, Koop T, et al. 2015. Size dependence of phase transitions in aerosol nanoparticles. *Nature*
630 *Communications* [J], 6(1): 5923.
- 631 Chrit M, Sartelet K, Sciare J, et al. 2018. Modeling organic aerosol concentrations and properties during
632 winter 2014 in the northwestern Mediterranean region. *Atmos. Chem. Phys.* [J], 18(24): 18079-
633 18100.
- 634 Chu B, Kerminen V-M, Bianchi F, et al. 2019. Atmospheric new particle formation in China. *Atmospheric*
635 *Chemistry and Physics* [J], 19(115-138.



- 636 Dal Maso M, Kulmala M, Riipinen I, et al. 2005. Formation and growth of fresh atmospheric aerosols:
637 Eight years of aerosol size distribution data from SMEAR II, Hyytiälä, Finland. *Boreal*
638 *Environment Research [J]*, 10(323-336).
- 639 Davidovits P, Worsnop D R, Jayne J T, et al. 2004. Mass accommodation coefficient of water vapor on
640 liquid water. *Geophysical Research Letters [J]*, 31(22).
- 641 Donahue N M, Robinson A L, Stanier C O, et al. 2006. Coupled Partitioning, Dilution, and Chemical Aging
642 of Semivolatile Organics. *Environmental Science & Technology [J]*, 40(8): 2635-2643.
- 643 Dong C, Matsui H, Spak S, et al. 2019. Impacts of New Particle Formation on Short-term Meteorology
644 and Air Quality as Determined by the NPF-explicit WRF-Chem in the Midwestern United States.
645 *Aerosol and Air Quality Research [J]*, 19(2): 204-220.
- 646 Dusek U, Frank G P, Hildebrandt L, et al. 2006. Size Matters More Than Chemistry for Cloud-Nucleating
647 Ability of Aerosol Particles. *Science [J]*, 312(5778): 1375-1378.
- 648 Ehn M, Thornton J, Kleist E, et al. 2014. A large source of low-volatility secondary organic aerosol. *Nature*
649 *[J]*, 506(476-479).
- 650 Fanourgakis G S, Kanakidou M, Nenes A, et al. 2019. Evaluation of global simulations of aerosol particle
651 and cloud condensation nuclei number, with implications for cloud droplet formation. *Atmos.*
652 *Chem. Phys. [J]*, 19(13): 8591-8617.
- 653 Gordon H, Kirkby J, Baltensperger U, et al. 2017. Causes and importance of new particle formation in
654 the present-day and preindustrial atmospheres. *122(16): 8739-8760.*
- 655 Grell G A 1993. Prognostic Evaluation of Assumptions Used by Cumulus Parameterizations. *Monthly*
656 *Weather Review [J]*, 121(3): 764-787.
- 657 Guo S, Hu M, Zamora M L, et al. 2014. Elucidating severe urban haze formation in China. *Proceedings of*
658 *the National Academy of Sciences [J]*, 111(49): 17373-17378.
- 659 Hong S-Y, Noh Y, Dudhia J 2006. A New Vertical Diffusion Package with an Explicit Treatment of
660 Entrainment Processes. *Monthly Weather Review - MON WEATHER REV [J]*, 134(
661 Hudson J G, Noble S 2014. CCN and Vertical Velocity Influences on Droplet Concentrations and
662 Supersaturations in Clean and Polluted Stratus Clouds. *Journal of the Atmospheric Sciences [J]*,
663 71(1): 312-331.
- 664 Iacono M, Delamere J, Mlawer E, et al. 2008. Radiative Forcing by Long-Lived Greenhouse Gases:
665 Calculations with the AER Radiative Transfer Models. *Journal of Geophysical Research [J]*, 113(
666 Jimenez J L, Canagaratna M R, Donahue N M, et al. 2009. Evolution of Organic Aerosols in the
667 Atmosphere. *Science [J]*, 326(5959): 1525-1529.
- 668 Kalkavouras P, Bougiatioti A, Kalivitis N, et al. 2019. Regional new particle formation as modulators of
669 cloud condensation nuclei and cloud droplet number in the eastern Mediterranean. *Atmos.*
670 *Chem. Phys. [J]*, 19(9): 6185-6203.
- 671 Kerminen V-M, Chen X, Vakkari V, et al. 2018. Atmospheric new particle formation and growth: Review
672 of field observations. *Environmental Research Letters [J]*, 13(
673 Krechmer J E, Day D A, Ziemann P J, et al. 2017. Direct Measurements of Gas/Particle Partitioning and
674 Mass Accommodation Coefficients in Environmental Chambers. *Environ Sci Technol [J]*, 51(20):
675 11867-11875.
- 676 Kulmala M, Dada L, Daellenbach K R, et al. 2021. Is reducing new particle formation a plausible solution
677 to mitigate particulate air pollution in Beijing and other Chinese megacities? *Faraday*
678 *Discussions [J]*, 226(0): 334-347.



- 679 Kulmala M, L L, Lehtinen K, et al. 2004. Initial steps of aerosol growth. *Atmospheric Chemistry and*
680 *Physics* [J], 4(
681 Kulmala M, Petäjä T, Ehn M, et al. 2013. Chemistry of Atmospheric Nucleation: On the Recent Advances
682 on Precursor Characterization and Atmospheric Cluster Composition in Connection with
683 Atmospheric New Particle Formation. *Annual review of physical chemistry* [J], 65(
684 Kulmala M, Petäjä T, Nieminen T, et al. 2012. Measurement of the nucleation of atmospheric aerosol
685 particles. *Nature Protocols* [J], 7(9): 1651-1667.
686 Lai S, Hai S, Gao Y, et al. 2022. The striking effect of vertical mixing in the planetary boundary layer on
687 new particle formation in the Yangtze River Delta. *Science of The Total Environment* [J],
688 829(154607).
689 Lee S-H, Gordon H, Yu H, et al. 2019. New Particle Formation in the Atmosphere: From Molecular
690 Clusters to Global Climate. *Journal of Geophysical Research: Atmospheres* [J], 124(
691 Li K, Zhu Y, Gao H, et al. 2015. A comparative study of cloud condensation nuclei measured between
692 non-heating and heating periods at a suburb site of Qingdao in the North China. *Atmospheric*
693 *Environment* [J], 112(40-53).
694 Li M, Liu H, Geng G, et al. 2017. Anthropogenic emission inventories in China: a review. *National Science*
695 *Review* [J], 4(6): 834-866.
696 Li X, Li Y, Cai R, et al. 2022. Insufficient Condensable Organic Vapors Lead to Slow Growth of New
697 Particles in an Urban Environment. *Environmental Science & Technology* [J], 56(14): 9936-9946.
698 Liu H J, Zhao C S, Nekat B, et al. 2014a. Aerosol hygroscopicity derived from size-segregated chemical
699 composition and its parameterization in the North China Plain. *Atmos. Chem. Phys.* [J], 14(5):
700 2525-2539.
701 Liu M, Matsui H 2022. Secondary Organic Aerosol Formation Regulates Cloud Condensation Nuclei in
702 the Global Remote Troposphere. *Geophysical Research Letters* [J], 49(18): e2022GL100543.
703 Liu X, Zhu Y, Zheng M, et al. 2014b. Production and growth of new particles during two cruise campaigns
704 in the marginal seas of China. *Atmospheric Chemistry and Physics* [J], 14(
705 Liu X H, Zhu Y J, Zheng M, et al. 2014c. Production and growth of new particles during two cruise
706 campaigns in the marginal seas of China. *Atmos. Chem. Phys.* [J], 14(15): 7941-7951.
707 Lovejoy E R, Curtius J, Froyd K D 2004. Atmospheric ion-induced nucleation of sulfuric acid and water.
708 *Journal of Geophysical Research: Atmospheres* [J], 109(D8).
709 Lu H, Wang G, Guo H 2022. Ambient acidic ultrafine particles in different land-use areas in two
710 representative Chinese cities. *Science of The Total Environment* [J], 830(154774).
711 Lu Y, Yan C, Fu Y, et al. 2019. A proxy for atmospheric daytime gaseous sulfuric acid concentration in
712 urban Beijing. *Atmos. Chem. Phys.* [J], 19(3): 1971-1983.
713 Lupascu A, Easter R, Zaveri R, et al. 2015. Modeling particle nucleation and growth over northern
714 California during the 2010 CARES campaign. *Atmos. Chem. Phys.* [J], 15(21): 12283-12313.
715 Ma N, Zhao C, Tao J, et al. 2016. Variation of CCN activity during new particle formation events in the
716 North China Plain. *Atmos. Chem. Phys.* [J], 16(13): 8593-8607.
717 Matsui H, Koike M, Kondo Y, et al. 2011. Impact of new particle formation on the concentrations of
718 aerosols and cloud condensation nuclei around Beijing. *Journal of Geophysical Research:*
719 *Atmospheres* [J], 116(D19).
720 Matsui H, Koike M, Takegawa N, et al. 2013. Spatial and temporal variations of new particle formation
721 in East Asia using an NPF-explicit WRF-chem model: North-south contrast in new particle
722 formation frequency. 118(20): 11,647-611,663.



- 723 Merikanto J, Spracklen D V, Mann G W, et al. 2009. Impact of nucleation on global CCN. *Atmos. Chem.*
724 *Phys. [J]*, 9(21): 8601-8616.
- 725 Mikkonen S, Romakkaniemi S, Smith J N, et al. 2011. A statistical proxy for sulphuric acid concentration.
726 *Atmos. Chem. Phys. [J]*, 11(21): 11319-11334.
- 727 Morrison H, Thompson G, Tatarskii V 2009. Impact of Cloud Microphysics on the Development of Trailing
728 Stratiform Precipitation in a Simulated Squall Line: Comparison of One and Two-Moment
729 Schemes. *Monthly Weather Review - MON WEATHER REV [J]*, 137(991-1007).
- 730 Nieminen T, Kerminen V M, Petäjä T, et al. 2018. Global analysis of continental boundary layer new
731 particle formation based on long-term measurements. *Atmos. Chem. Phys. [J]*, 18(19): 14737-
732 14756.
- 733 Petäjä T, Mauldin I R L, Kosciuch E, et al. 2009. Sulfuric acid and OH concentrations in a boreal forest
734 site. *Atmos. Chem. Phys. [J]*, 9(19): 7435-7448.
- 735 Pierce J, Riipinen I, Kulmala M, et al. 2011. Quantification of the volatility of secondary organic
736 compounds in ultrafine particles during nucleation events. *Atmospheric Chemistry and Physics*
737 *Discussions [J]*, 11(14495-14539).
- 738 Pöschl U, Canagaratna M, Jayne J T, et al. 1998. Mass Accommodation Coefficient of H₂SO₄ Vapor on
739 Aqueous Sulfuric Acid Surfaces and Gaseous Diffusion Coefficient of H₂SO₄ in N₂/H₂O. *The*
740 *Journal of Physical Chemistry A [J]*, 102(49): 10082-10089.
- 741 Qiao X, Yan C, Li X, et al. 2021. Contribution of Atmospheric Oxygenated Organic Compounds to Particle
742 Growth in an Urban Environment. *Environmental Science & Technology [J]*, XXXX(
- 743 Ren J, Chen L, Fan T, et al. 2021. The NPF Effect on CCN Number Concentrations: A Review and Re-
744 Evaluation of Observations From 35 Sites Worldwide. *Geophysical Research Letters [J]*, 48(19):
745 e2021GL095190.
- 746 Riipinen I, Sihto S L, Kulmala M, et al. 2007. Connections between atmospheric sulphuric acid and new
747 particle formation during QUEST III‐IV campaigns in Heidelberg and Hyytiälä. *Atmos.*
748 *Chem. Phys. [J]*, 7(8): 1899-1914.
- 749 Roldin P, Swietlicki E, Massling A, et al. 2011a. Aerosol ageing in an urban plume – implication for climate.
750 *Atmos. Chem. Phys. [J]*, 11(12): 5897-5915.
- 751 Roldin P, Swietlicki E, Schurgers G, et al. 2011b. Development and evaluation of the aerosol dynamics
752 and gas phase chemistry model ADCHEM. *Atmos. Chem. Phys. [J]*, 11(12): 5867-5896.
- 753 Saha S, Moorthi S, Wu X, et al. 2014. The NCEP Climate Forecast System Version 2. *Journal of Climate*
754 *[J]*, 27(6): 2185-2208.
- 755 Shrivastava M, Fast J, Easter R, et al. 2011. Modeling organic aerosols in a megacity: comparison of
756 simple and complex representations of the volatility basis set approach. *Atmospheric*
757 *Chemistry and Physics [J]*, 11(6639-6662).
- 758 Shrivastava M K, Lane T E, Donahue N M, et al. 2008. Effects of gas particle partitioning and aging of
759 primary emissions on urban and regional organic aerosol concentrations. 113(D18).
- 760 Sihto S L, Kulmala M, Kerminen V M, et al. 2006. Atmospheric sulphuric acid and aerosol formation:
761 implications from atmospheric measurements for nucleation and early growth mechanisms.
762 *Atmos. Chem. Phys. [J]*, 6(12): 4079-4091.
- 763 Sihto S L, Mikkilä J, Vanhanen J, et al. 2011. Seasonal variation of CCN concentrations and aerosol
764 activation properties in boreal forest. *Atmos. Chem. Phys. [J]*, 11(24): 13269-13285.
- 765 Tewari M, Wang W, Dudhia J, et al. 2016. Implementation and verification of the united NOAA land
766 surface model in the WRF model [M].



- 767 Virtanen A, Kannosto J, Kuuluvainen H, et al. 2011. Bounce behavior of freshly nucleated biogenic
768 secondary organic aerosol particles. *Atmos. Chem. Phys.* [J], 11(16): 8759-8766.
- 769 Wang D-W, Guo H, Chan C K 2014. Diffusion Sampler for Measurement of Acidic Ultrafine Particles in
770 the Atmosphere. *Aerosol Science and Technology* [J], 48(12): 1236-1246.
- 771 Wang J, Li M, Li L, et al. 2022. Particle number size distribution and new particle formation in Xiamen,
772 the coastal city of Southeast China in wintertime. *Science of The Total Environment* [J],
773 826(154208).
- 774 Westervelt D M, Pierce J R, Riipinen I, et al. 2013. Formation and growth of nucleated particles into
775 cloud condensation nuclei: model-measurement comparison. *Atmos. Chem. Phys.* [J], 13(15):
776 7645-7663.
- 777 Wu H, Li Z, Jiang M, et al. 2021a. Contributions of traffic emissions and new particle formation to the
778 ultrafine particle size distribution in the megacity of Beijing. *Atmospheric Environment* [J],
779 262(118652).
- 780 Wu L, Ling Z, Shao M, et al. 2021b. Roles of Semivolatile/Intermediate-Volatility Organic Compounds on
781 SOA Formation Over China During a Pollution Episode: Sensitivity Analysis and Implications for
782 Future Studies. *Journal of Geophysical Research: Atmospheres* [J], 126(8): e2020JD033999.
- 783 Wu Z, Hu M, Yue D, et al. 2011. Evolution of particle number size distribution in an urban atmosphere
784 during episodes of heavy pollution and new particle formation. *Science China Earth Sciences*
785 [J], 54(11): 1772.
- 786 Yao L, Garmash O, Bianchi F, et al. 2018. Atmospheric new particle formation from sulfuric acid and
787 amines in a Chinese megacity. *Science* [J], 361(278-281).
- 788 Yu F 2005. Quasi-unary homogeneous nucleation of H₂SO₄ - H₂O. *The Journal of Chemical Physics* [J],
789 122(7): 074501.
- 790 Yu F, Luo G, Nair A A, et al. 2020. Wintertime new particle formation and its contribution to cloud
791 condensation nuclei in the Northeastern United States. *Atmos. Chem. Phys.* [J], 20(4): 2591-
792 2601.
- 793 Yu F, Luo G, Pryor S C, et al. 2015. Spring and summer contrast in new particle formation over nine forest
794 areas in North America. *Atmos. Chem. Phys.* [J], 15(24): 13993-14003.
- 795 Yuan Q, Li W, Zhou S, et al. 2015. Integrated evaluation of aerosols during haze-fog episodes at one
796 regional background site in North China Plain. *Atmospheric Research* [J], 156(102-110).
- 797 Yue D L, Hu M, Zhang R Y, et al. 2011. Potential contribution of new particle formation to cloud
798 condensation nuclei in Beijing. *Atmospheric Environment* [J], 45(33): 6070-6077.
- 799 Zaveri R A, Easter R C, Fast J D, et al. 2008. Model for Simulating Aerosol Interactions and Chemistry
800 (MOSAIC). 113(D13).
- 801 Zaveri R A, Easter R C, Peters L K 2005. A computationally efficient Multicomponent Equilibrium Solver
802 for Aerosols (MESA). *Journal of Geophysical Research: Atmospheres* [J], 110(D24).
- 803 Zhang Q, Jimenez J L, Canagaratna M R, et al. 2007. Ubiquity and dominance of oxygenated species in
804 organic aerosols in anthropogenically-influenced Northern Hemisphere midlatitudes.
805 *Geophysical Research Letters* [J], 34(13).
- 806 Zhao B, Wang S, Donahue N M, et al. 2016. Quantifying the effect of organic aerosol aging and
807 intermediate-volatility emissions on regional-scale aerosol pollution in China. *Scientific*
808 *Reports* [J], 6(1): 28815.
- 809 Zheng B, Tong D, Li M, et al. 2018. Trends in China's anthropogenic emissions since 2010 as the
810 consequence of clean air actions. *Atmos. Chem. Phys.* [J], 18(19): 14095-14111.



811 Zhu Y, Li K, Shen Y, et al. 2019. New particle formation in the marine atmosphere during seven cruise
812 campaigns. *Atmos. Chem. Phys. [J]*, 19(1): 89-113.
813 Zhu Y, Sabaliauskas K, Liu X, et al. 2014. Comparative analysis of new particle formation events in less
814 and severely polluted urban atmosphere. *Atmospheric Environment [J]*, 98(655-664).
815 Zhu Y, Shen Y, Li K, et al. 2021. Investigation of Particle Number Concentrations and New Particle
816 Formation With Largely Reduced Air Pollutant Emissions at a Coastal Semi-Urban Site in
817 Northern China. *Journal of Geophysical Research: Atmospheres [J]*, 126(17): e2021JD035419.
818
819